

# RSC Advances



This is an *Accepted Manuscript*, which has been through the Royal Society of Chemistry peer review process and has been accepted for publication.

*Accepted Manuscripts* are published online shortly after acceptance, before technical editing, formatting and proof reading. Using this free service, authors can make their results available to the community, in citable form, before we publish the edited article. This *Accepted Manuscript* will be replaced by the edited, formatted and paginated article as soon as this is available.

You can find more information about *Accepted Manuscripts* in the [Information for Authors](#).

Please note that technical editing may introduce minor changes to the text and/or graphics, which may alter content. The journal's standard [Terms & Conditions](#) and the [Ethical guidelines](#) still apply. In no event shall the Royal Society of Chemistry be held responsible for any errors or omissions in this *Accepted Manuscript* or any consequences arising from the use of any information it contains.

# Hybrid silver nanoparticles/nanoclusters-decorated polypyrrole for high-performance supercapacitors

John Kevin Gan,<sup>1</sup> Yee Seng Lim,<sup>1</sup> Nay Ming Huang,<sup>1\*</sup> Hong Ngee Lim<sup>2,3</sup>

<sup>1</sup>Low Dimensional Materials Research Centre, Department of Physics, Faculty of Science, University of Malaya, 50603 Kuala Lumpur, Malaysia

<sup>2</sup>Department of Chemistry, Faculty of Science, Universiti Putra Malaysia, 43400 UPM Serdang, Selangor, Malaysia

<sup>3</sup>Functional Device Laboratory, Institute of Advanced Technology, Universiti Putra Malaysia, 43400 UPM Serdang, Selangor, Malaysia

Corresponding author: huangnayming@um.edu.my (Huang N.M.)

## Abstract

In the present work, a composite electrode consisting of hybrid silver nanoparticles/nanoclusters-decorated polypyrrole (PPy) demonstrates an enhanced specific capacitance of 414 F g<sup>-1</sup> than that of the pure PPy electrode (273 F g<sup>-1</sup>). The enhanced specific capacitance was mainly attributed to the unique architecture and hybrid nanostructures of Ag. The Ag nanoparticles enhanced the electron hopping system of the PPy, effectively increasing the capacitance properties of the PPy. On the other hand, the Ag nanoclusters acted as spacers to prevent the restacking of PPy films, further extending the active sites for redox reactions, leading to improved specific capacitance. A symmetric supercapacitor device built from the hybrid Ag@PPy nanocomposite yielded a specific capacitance of 161 F g<sup>-1</sup> per mass of one electrode and exhibited remarkable cycling stability of 98.9% capacitance retention over 1000 charge/discharge cycles. These excellent electrochemical performances show the promise of hybrid Ag@PPy nanocomposite in energy storage devices.

## 1. Introduction

Supercapacitors or electrochemical capacitors have a wide array of applications, including starters, consumer electronics, military defence systems and power back-up systems.<sup>1,2</sup> Supercapacitors have attracted great attention due to their superior fast charging and discharging process, long cycle life and environmental friendliness.<sup>3-5</sup> They offer a higher energy density than conventional capacitors and a higher power density than batteries.<sup>6</sup>

Supercapacitors can be classified into two categories; electric double layer capacitors (EDLC) and pseudocapacitors. EDLC store charges by non-faradaic charge separation at the electrode/electrolyte interface. Carbon-based materials are usually employed as electrode materials in EDLC. On the other hand, pseudocapacitors undergo fast and reversible faradaic reaction between electrolyte and electrode. Recently, much attention has been shifted to pseudocapacitors as they possess relatively higher capacitances as compared to carbon-based materials.<sup>7</sup> The charge storage mechanisms of pseudocapacitors are based on the faradaic redox reactions that occur at the interface between the electrode and electrolyte. Pseudocapacitor materials include conducting polymers like polypyrrole (PPy), polyaniline (PANI) and several transition metal oxides, including  $V_2O_5$ ,<sup>8</sup>  $NiO$ ,<sup>9</sup>  $MnO_2$ <sup>10</sup> and  $Co_3O_4$ .<sup>11</sup> Among pseudocapacitor materials, conducting polymers offer the advantages of higher charge density compared to carbon materials and lower cost in contrast to metal oxides.<sup>12</sup>

Among the available conducting polymers, PPy is one of the most studied conducting polymers as pseudocapacitor materials. PPy, which contains a conjugated structure of alternating C=C double bonds has recently garnered much attention due to its greater degree electrochemical processing flexibility, light weight, and high electrical conductivity than

most other commercially available conducting polymers.<sup>13</sup> The main drawback of using conducting polymers as supercapacitor electrodes is their poor stability during cycling when used as bulk materials. The conducting polymers films undergo swelling, shrinking, cracks or breaking during the doping-dedoping process (insertion/deinsertion of counter ions). These processes gradually aggravate their conducting properties.<sup>3,14</sup> To overcome this problem, researches have focused on synthesizing PPy/carbon based composites such as activated carbon,<sup>15</sup> carbon nanotubes<sup>16</sup> and graphene.<sup>17</sup> Also, the synergistic effects of PPy/metal oxides composite electrodes have been applied as electrode for supercapacitor applications.<sup>18,19</sup> Another effective way to enhance the electronic conductivity of PPy is by metal doping.<sup>20-22</sup>

Recently, PPy hybrids with silver have been prepared from various methods for different application studies. Zhao *et al.* have synthesized nanofiber-like Ag@PPy core-shell structure from silver nitrate and pyrrole in the presence of sodium dodecyl benzyl sulfonate (SDBS). They investigated the effects of the concentration of SDBS on the morphology and the electrical conductivity of the composites.<sup>23</sup> PPy-Ag nanowire has been synthesized by Hnida *et al.* via cathodic co-deposition and its use in hydrogen peroxide sensing.<sup>24</sup> Yang *et al.* have reported the formation of PPy-Ag composite nanotubes in the presence of polyvinylpyrrolidone (PVP) and its chemiresistor response to ammonia.<sup>25</sup>

PPy/Ag composites used as electrode materials for supercapacitors applications are worthwhile to explore considering the highly electrically conductive Ag metal that may mediate the effective charge migration through the PPy. However, there have been a limited number of studies on the supercapacitor application of PPy/Ag composites. In a recent study, Patil *et al.* synthesized PPy/polyacrylic acid (PAA)/Ag composite electrodes for supercapacitor application.<sup>12</sup> The PPy/PAA/Ag electrodes were prepared via a series of steps involving the polymerization of pyrrole using oxidant, preparing a solution mixture of PPy,

PAA and silver nitrate, followed by dip coating of the substrate into the solution mixture. Although supercapacitance of the composite electrode was enhanced due to the incorporation of Ag, the pre-synthesized PPy bulk particles do not have sufficient surface area for the incorporation of Ag nanoparticles on a nanoscale level as only the outer surface of the PPy particles are decorated with Ag nanoparticles. This approach reduces the practical specific capacitance of the PPy. Hence, substantial improvements have to be made for its commercialization.

In this study, we report a facile route to synthesize a unique hybrid Ag nanoparticles/nanoclusters-decorated PPy electrode. Herein, we report for the first time the formation of hybrid Ag nanoparticles/nanoclusters compositing with PPy via *in-situ* redox reaction followed by electrodeposition. The influence of the AgNO<sub>3</sub> concentrations on the formation of Ag nanoparticles/nanoclusters and their electrochemical performances were also investigated. Three- and two- electrode configurations were used to study the electrochemical performances of the hybrid Ag@PPy nanocomposite electrodes.

## 2. Experimental Methods

### 2.1 Materials

Pyrrole (99%) was purchased from Acros Organic, stored at 0 °C, and distilled prior to use. Silver nitrate ( $\text{AgNO}_3$ ) and sodium p-toluenesulfonate (NapTS, 98%) were purchased from Merck. Sulfuric acid ( $\text{H}_2\text{SO}_4$ , 98%) was purchased from System. Graphite sheet was purchased from Latech.

### 2.2 Synthesis of Ag@PPy nanocomposites

The Ag@PPy nanocomposites were prepared by the *in-situ* reaction between pyrrole and  $\text{AgNO}_3$  followed by electrochemical polymerization from an aqueous solution placed in a one-compartment cell. The deposition solution that contained 0.1 M pyrrole, 0.1 M NapTS and 0.05 M  $\text{AgNO}_3$ , was stirred vigorously for 5 min to allow the redox reaction between the pyrrole and  $\text{Ag}^+$ . A piece of graphite sheet (1 x 1 cm) was then immersed into the deposition solution and the Ag@PPy was deposited at a constant potential of +0.8 V. All the potentials were referenced to a saturated calomel electrode (SCE) and a platinum wire was used as the auxiliary electrode. The deposition was stopped when the accumulated charge reaches 4 C with a mass loading of ~2.3 mg. The as-prepared electrodes were denoted as xM-Ag@PPy, where x depicts the concentration of the  $\text{AgNO}_3$  used. When only Ag@PPy is mentioned, it is prepared at 0.05 M.

### 2.3 Materials characterization

The Fourier transform infrared (FTIR) spectra of the hybrid Ag@PPy nanocomposites were recorded on a Perkin-Elmer FT-IR spectroscope (model 1725x), and the Raman spectra were measured using a Reinshaw inVia Raman microscope with green laser excitation (514 nm). The morphologies of the prepared samples were examined using a field emission scanning electron microscopy (FESEM, FEI Quanta SEM Model 400F). High resolution transmission

electron microscopy (HRTEM) was carried out using JEOL JEM2100-F. X-ray photoelectron spectroscopy (XPS) measurements were performed using synchrotron radiation from beam line 3.2 at the Synchrotron Light Research Institute, Thailand.

#### 2.4 Electrochemical characterization

To understand the electrochemical performance of the Ag@PPy nanocomposite electrode, the electrochemical properties of the materials were measured using Gamry Reference 600. The electrochemical measurements were carried out in a three-electrode system that consists of a Ag@PPy nanocomposite as the working electrode, a platinum wire as the auxiliary electrode and SCE as the reference electrode. All electrochemical measurements were carried in 1.0 M H<sub>2</sub>SO<sub>4</sub> electrolyte. The specific capacitance was calculated from the galvanostatic charge/discharge (GCD) curves using equations (1).

$$C_m = I\Delta t/m\Delta V \quad (1)$$

where  $C_m$  is the specific capacitance in farads per gram,  $I$  is the discharge current,  $\Delta t$  is the discharge time,  $m$  is the mass of the active materials in the electrode and  $\Delta V$  is the potential window. Electrochemical impedance spectroscopy (EIS) was carried out with a perturbation amplitude of 5 mV versus the open-circuit potential within a frequency range of 100 kHz to 10 mHz.

#### 2.5 Supercapacitor device testing

A two-electrode cell was assembled using a Teflon Swagelok® construction with two Ag@PPy nanocomposite electrodes fabricated by the same method mentioned above and a piece of filter paper soaked with 1.0 M H<sub>2</sub>SO<sub>4</sub> electrolyte was used as separator. The specific capacitance per mass of one electrode is calculated according to equation (2)

$$C_m = 2C/m \quad (2)$$

where  $C$  is the experimental measured capacitance of the supercapacitor device, and  $m$  is the mass of one Ag@PPy electrode. The energy and power density of the symmetric supercapacitor were calculated from the GCD measurements by employing equations (3) and (4), respectively.

$$E_{cell} = \frac{1}{2} C_{cell} V^2 \quad (3)$$

$$P_{cell} = E_{cell} / \Delta t \quad (4)$$

where  $E_{cell}$  is the energy density ( $\text{W h kg}^{-1}$ ),  $C_{cell}$  is the specific capacitance of the cell,  $V$  is the working potential window,  $P_{cell}$  is the power density ( $\text{W kg}^{-1}$ ), and  $\Delta t$  is the discharge time.

### 3. Results and Discussion

#### 3.1 Synthesis and formation mechanism

In this study, the formation of the Ag@PPy nanocomposite took place via a facile *in-situ* redox reaction of pyrrole and AgNO<sub>3</sub>, in which the Ag<sup>+</sup> was reduced to Ag and pyrrole was oxidized to PPy in the absence of any stabilizer or surfactant. The recent work of Amarnath *et al.* showed that pyrrole can act as a reducing agent.<sup>26</sup> When AgNO<sub>3</sub> is added into the pyrrole solution, pyrrole monomers will oxidize to form the radical cations of pyrrole monomer, releasing free electrons during the process. The Ag<sup>+</sup> ions are subsequently reduced to Ag particles by the free electrons released during the formation of free radicals. The coupling process between two cation radicals followed by the expelling of two protons resulted in the generation of an aromatic dimer. The propagation step continues via the oxidation, coupling and deprotonation processes. Even though the reaction mixture of pyrrole and AgNO<sub>3</sub> was only allowed to stir for 5 min, color change can already be observed in the

reaction vessel as shown in Fig. 1. We believe that it is due to the formation of pyrrole oligomers. The stirring time is kept short to prevent the oligomers from propagating into solid PPy, as solid PPy is not suitable for electrodeposition. Finally, the propagation step is continued via electrodeposition to deposit Ag@PPy nanocomposite onto a graphite sheet.

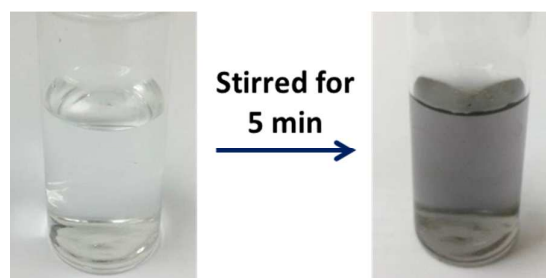


**Fig. 1** Physical appearance of the reaction mixture after stirring for 5 min prior to electrodeposition.

### 3.2 FTIR and Raman analysis

Fig. 2a shows the FTIR spectrum of the Ag@PPy nanocomposite. The N-H and C-H stretching peaks were located at 3340 and 3000  $\text{cm}^{-1}$ , respectively. The band at 1622  $\text{cm}^{-1}$  was corresponded to the C=C/C-C vibration of the pyrrole ring, while the band at 1399  $\text{cm}^{-1}$  was contributed by the pyrrole ring vibration. C-N in plane formation can be observed at 1260  $\text{cm}^{-1}$ .<sup>27,28</sup> The bands at 1096 and 982  $\text{cm}^{-1}$  can be attributed to N-H in plane deformation vibration and the C-H out-of-plane vibration, respectively, implying the doping state of PPy.<sup>29</sup>

The Raman spectra of pure PPy and Ag@PPy are shown in Fig. 2b. The characteristic bands at 1575 and 1385  $\text{cm}^{-1}$  are assigned to the ring stretching mode and C=C backbone stretching of PPy, respectively. For the pure PPy, the band at 1055  $\text{cm}^{-1}$  is attributed to the

symmetrical C-H in plane bending. In addition, the two bands at 975 and 935  $\text{cm}^{-1}$  are due to the bipolaron ring and polaron structure.<sup>30</sup> The characteristic absorption peaks of PPy are also exhibited in Ag@PPy with little alteration of the bands, which indicates the presence of the unchanged internal structure of the PPy in the composite.

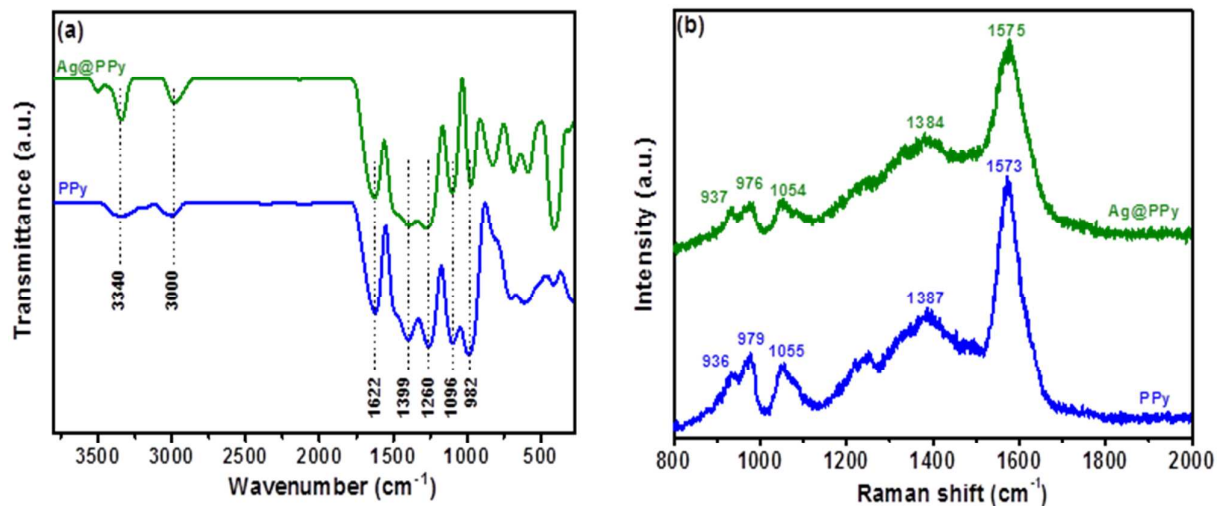
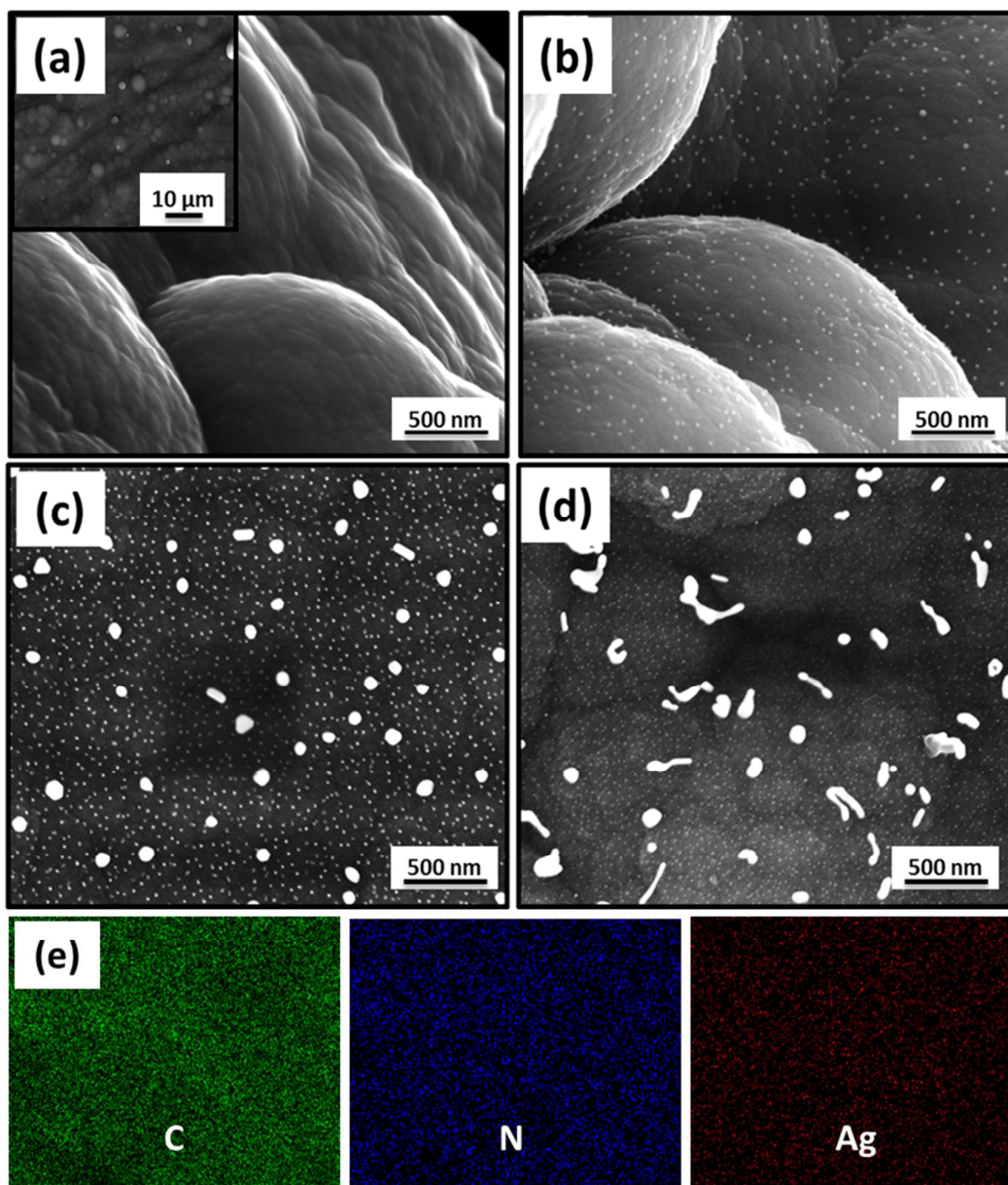


**Fig. 2** (a) FTIR and (b) Raman spectra of PPy and Ag@PPy.

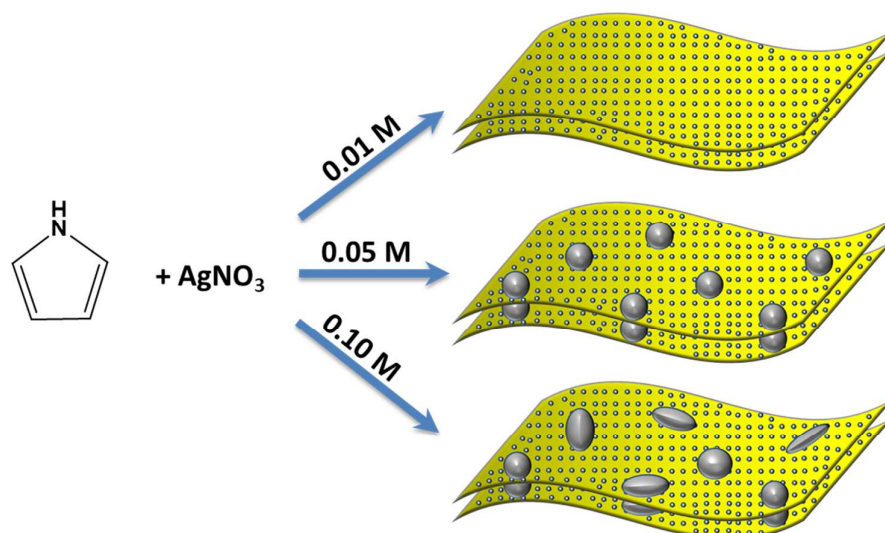
### 3.3 Morphological studies Ag@PPy nanocomposite

Fig. 3 shows the FESEM morphologies of the as-prepared samples. Fig. 3a shows the silver-free PPy film had typical cauliflower morphology and the higher magnification image shows a smooth PPy without any embedment of Ag nanoparticles. For 0.01M-Ag@PPy, small spherical Ag nanoparticles can be clearly seen on the surface of PPy as shown in Fig. 3b. Surprisingly, when the concentration of  $\text{AgNO}_3$  increased to 0.05 M, two different sizes of Ag were observed; Ag nanoparticles and Ag nanoclusters. The Ag nanoclusters with particle size ranging from 55-100 nm can be seen decorated evenly alongside the small Ag nanoparticles on the PPy film (Fig. 3c). We deduce that the small Ag nanoparticles were

already formed during the initial redox reaction between pyrrole and  $\text{Ag}^+$  ions prior to electrodeposition. During electrodeposition, the oxidizing role of  $\text{Ag}^+$  ions is replaced by the electrode oxidation process on the substrate when potential is applied. The excess  $\text{Ag}^+$  ions will selectively adsorbed onto the Ag nanoparticles surfaces because of ionic adsorption effect<sup>12</sup> and is subsequently reduced to Ag nanoclusters from the free electrons released during the continuous formation of radical pyrrole cations. The Ag nanoclusters tend to have irregular shapes with increased in their sizes when the  $\text{AgNO}_3$  concentration was further increased to 0.10 M as depicted in Fig. 3d. Elemental mapping was performed on the 0.05M- $\text{Ag@PPy}$  nanocomposite, as shown in Fig. 3e. The areas of bright contrast correlate to the distributions of C, N and Ag in the nanocomposite. The model for the formation of different  $\text{Ag@PPy}$  nanocomposite is shown in Scheme 1.



**Fig. 3** FESEM images of (a) pure PPy, inset showing PPy at lower magnification; Ag@PPy nanocomposites with AgNO<sub>3</sub> concentrations of (b) 0.01 M, (c) 0.05 M, (d) 0.10 M, and (e) elemental mapping of the 0.05M-Ag@PPy nanocomposite.



**Scheme 1** Schematic representation of the evolution of different Ag@PPy nanocomposites.

HRTEM images of the 0.05M-Ag@PPy nanocomposite are shown in Fig. 4. The Ag nanoclusters and Ag nanoparticles can be clearly seen in Fig. 4a and b, respectively. Fig. 4b clearly shows the deposition of distributed ultra-small Ag nanoparticles having a size range of 2-4 nm on the surface of the PPy film.

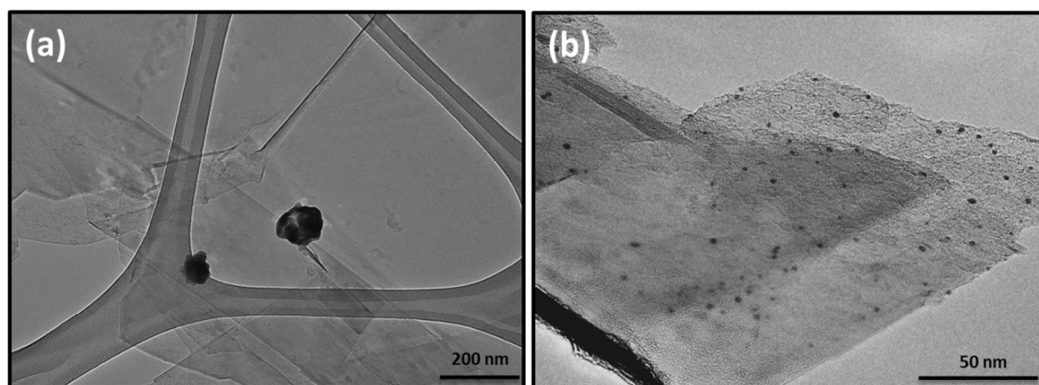


**Fig. 4** HRTEM images of (a) Ag nanoparticles and (b) Ag nanoclusters.

### 3.4 XPS analysis of hybrid Ag@PPy nanocomposite

XPS was used to characterize the chemical state of the as-prepared hybrid Ag@PPy nanocomposite and is shown in Fig. 5. Fig. 5a shows the N 1s core level spectrum of the Ag@PPy nanocomposite and could be deconvoluted into three peaks. The main peak at 399.1 eV was attributed to the neutral amine nitrogen (N-H). The peak at higher binding energy of 400.3 eV corresponds to the positively charged nitrogen ( $-N^+$ ). Another peak at the lower binding energy side (397.9 eV) can be assigned to the imine nitrogen ( $-N=$ ).<sup>31</sup> The Ag 3d core level spectrum of the Ag@PPy nanocomposite is shown in Fig. 5b. Two peaks are observed at 368.0 and 374.1 eV with 6.1 eV spin energy separations, corresponding to the binding energies of the Ag 3d<sub>5/2</sub> and Ag 3d<sub>3/2</sub> core levels, respectively.<sup>32</sup> The XPS analysis provided support for the existence of metallic silver in the nanocomposite materials.

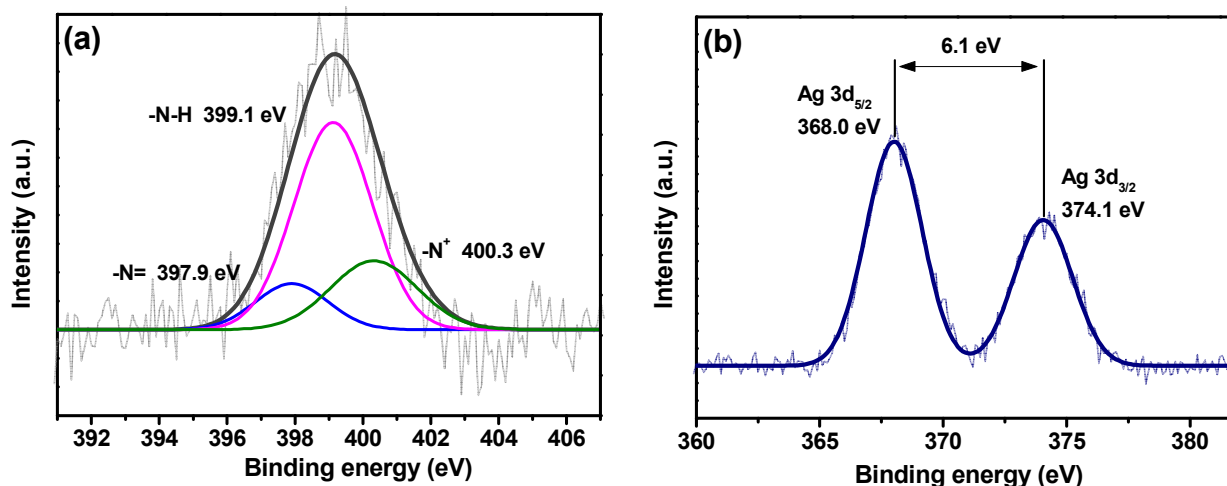


**Fig. 5** XPS spectra of Ag@PPy nanocomposite at (a) N 1s and (b) Ag 3d core level spectra.

### 3.5 Electrochemical characterizations of Ag@PPy nanocomposite

Cyclic voltammetry (CV) was used to evaluate the electrochemical performances of the as-prepared PPy and Ag@PPy nanocomposite electrodes. Fig. 6a shows the CV curves of the electrodes in 1.0 M H<sub>2</sub>SO<sub>4</sub> electrolyte at a scan rate of 10 mV s<sup>-1</sup>. It is apparent that the peak current was greatly enhanced for the Ag@PPy nanocomposite electrode as compared to that for the pure PPy electrode. No well-defined peaks were observed for the PPy electrode. Interestingly, two pairs of redox peaks were observed for the Ag@PPy nanocomposite electrode. For the Ag nanoparticles, the oxidation peak was observed at 0.19 V while the minute reduction peak was observed at around 0.01 V.<sup>33</sup> The second pair of redox peak was attributed by the oxidation and reduction of Ag nanoclusters, having broad anodic and cathodic peaks situated at 0.50 and 0.20 V, respectively.<sup>34</sup> Here we observed that redox behavior is affected by size. Also, the separation between the anodic and cathodic peaks increases with the size of Ag particles. These observations are in good agreement with previous studies.<sup>35,36</sup> The CV results imply the presence of hybrid Ag nanoparticles and Ag nanoclusters in the Ag@PPy nanocomposite.

Fig. 6b shows the GCD curves of the pure PPy and the Ag@PPy nanocomposite electrodes at current density of 0.2 A g<sup>-1</sup>. The GCD curve of Ag@PPy nanocomposite shows longer discharge time than the pure PPy, indicating that the Ag@PPy nanocomposite has better capacitance property than PPy. The specific capacitances of the electrodes were calculated from the GCD curves using eqn (1) at current density of 0.2 A g<sup>-1</sup>. A capacitance of 273 F g<sup>-1</sup> was found for the pure PPy and the capacitance improved to 414 F g<sup>-1</sup> with the incorporation of Ag nanoparticles and nanoclusters, which was almost a 52% increment in the specific capacitance. This shows that the addition of Ag nanoparticles improved the electron transfer in the Ag@PPy system. The metallic conductor Ag nanoparticles mediate

the electron hopping within the conjugated systems of the PPy chains, harnessing fully the capacitance properties of PPy while the anchored Ag nanoclusters acted as spacers to prevent the restacking of PPy films. Conversely, the thick and densely packed PPy electrode is undesirable for fast ion kinetics and attributes to decreased charge storage performance. The dependence of specific capacitance on current density for the PPy and hybrid Ag@PPy nanocomposite is shown in Fig. 6c. It can be observed that the specific capacitance of the hybrid Ag@PPy nanocomposite is much higher than that of pure PPy at all current densities. The specific capacitance for the hybrid Ag@PPy nanocomposite at  $10 \text{ A g}^{-1}$  remained high at  $206 \text{ F g}^{-1}$ ; this desirable feature of the electrode allows it to operate at a wide range of current densities.

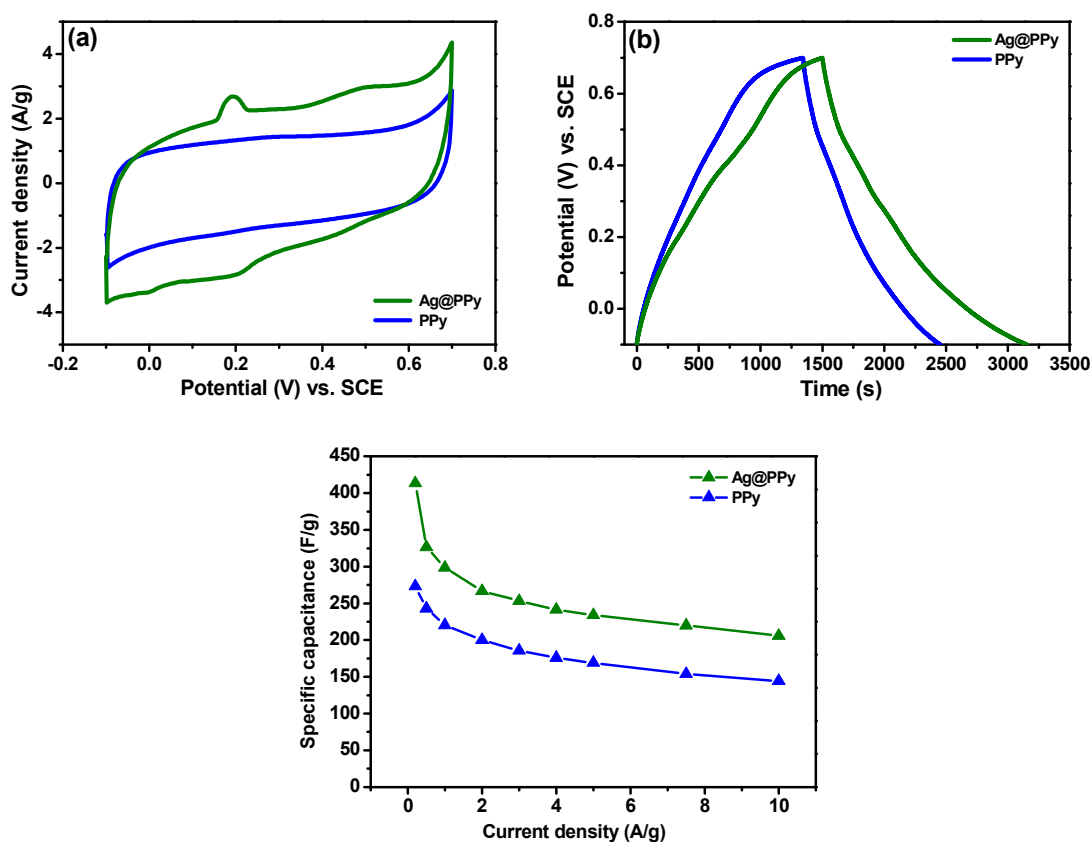


**Fig. 6** (a) CV curves at  $10 \text{ mV s}^{-1}$ , (b) GCD curves at  $0.2 \text{ A g}^{-1}$ , and (c) dependence of specific capacitance on current density for PPy and hybrid Ag@PPy nanocomposite electrode.

To ascertain the applicability of the electrodes for high-performance supercapacitors, CV curves of PPy and hybrid Ag@PPy nanocomposite electrode were recorded and compared at various scan rates. Fig. 7a and b show that the area under the curve increases as the scan rate increases. At their respective scan rates, the Ag@PPy nanocomposite electrode exhibited higher output current in comparison the PPy electrode, indicating an enhancement of charge storage in the composite electrode. Although the output currents of the PPy electrode was lower compared to that of the hybrid Ag@PPy nanocomposite electrode, the CV curves still exhibited quasi-rectangular shapes, revealing the good capacitance behavior and high-rate compatibility of PPy, making it a suitable platform for the anchoring of Ag nanoparticles/nanoclusters. As shown in Fig. 7b, with the increase of potential scan rate from 10 to 100  $\text{mV s}^{-1}$ , the anodic peak potential shifted to higher potentials and the cathodic peaks shifted to lower potentials. This is mainly due to the resistance of the electrode.<sup>37</sup> The shape of the CV curves was maintained even at high scan rates, indicating excellent capacitance behavior of the nanocomposite electrode.

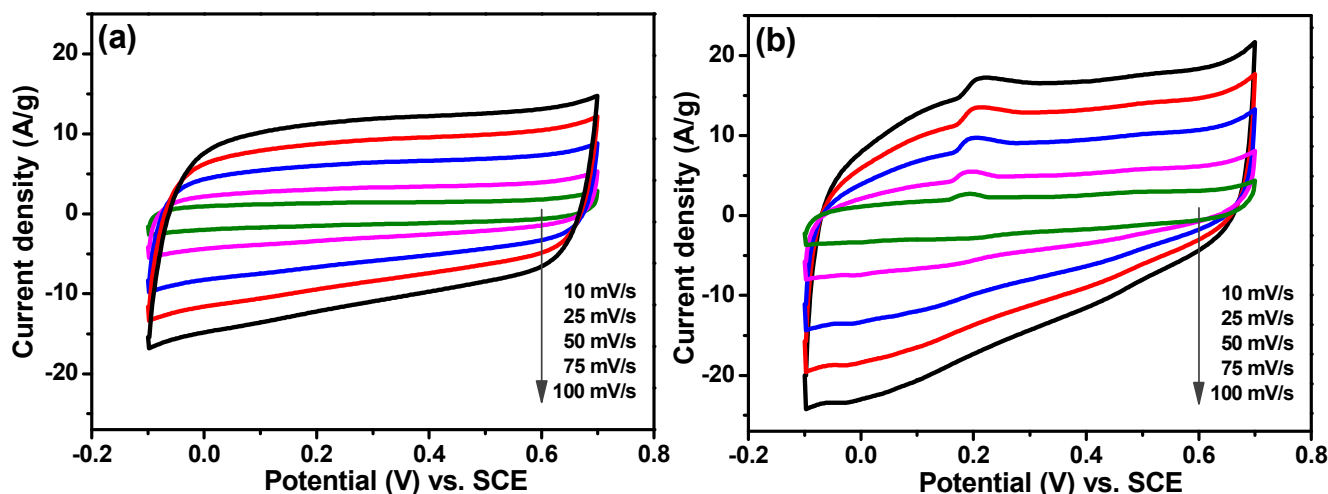


**Fig. 7** CV curves at various scan rates for (a) PPy, and (b) hybrid Ag@PPy nanocomposite electrode.

The optimization of Ag on PPy is essential from the economic and high-performance perspective for a supercapacitor. Hence, the electrochemical performances of the Ag@PPy nanocomposite electrodes prepared using different concentrations of AgNO<sub>3</sub> were evaluated. Fig. 8 shows the effect of AgNO<sub>3</sub> concentration on the electrochemical performance of nanocomposite. The specific capacitances increased from 273 F g<sup>-1</sup> to 414 F g<sup>-1</sup> when the AgNO<sub>3</sub> concentration was increased from 0 to 0.05 M. Then, a further increase in the AgNO<sub>3</sub> concentration eventually led to the decrease in specific capacitance. The decrease in the efficiency at high Ag loading is due to the free standing/excess Ag in the composite that may oxidized to Ag(I) and also may be eroded by the electrolyte.<sup>38</sup> As seen from the FESEM results, the Ag@PPy prepared from 0.10 M AgNO<sub>3</sub> has irregular and large Ag nanoclusters anchored on the nanocomposite which may lead to a decrease in the active surface area of PPy film, reducing its interaction with the electrolyte ions. Consequently, the overall supercapacitance performance of the electrode would have deteriorated.

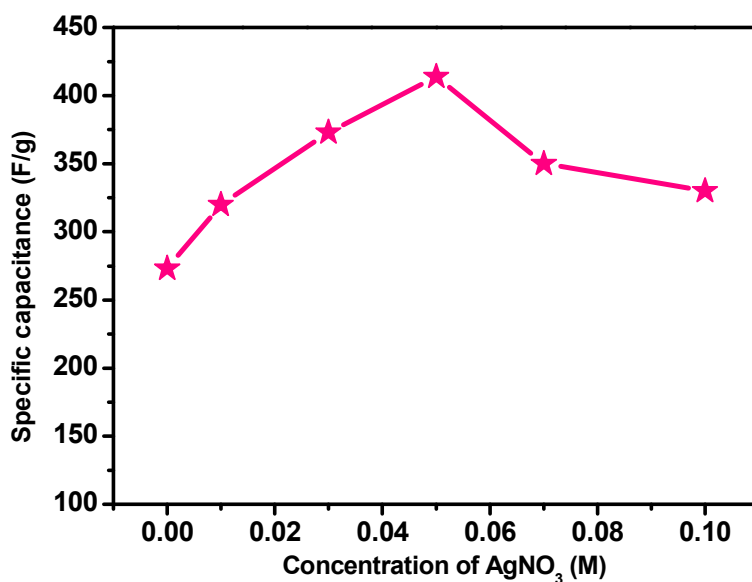


**Fig. 8** Specific capacitance values for different AgNO<sub>3</sub> concentrations calculated at current density of 0.2 A g<sup>-1</sup>.

The electrochemical impedance spectra (EIS) were recorded in a frequency range between 10 mHz and 100 kHz, as shown in Fig. 9. The first intercept of the semicircle at the real axis in the high frequency region represents the equivalent series resistance (ESR), which is attributed to the resistance of the electrolyte; the contact resistance between the electrolyte, current collector, and active material; and the intrinsic resistance of the active material itself. The ESR values were determined to be 0.679 and 0.149  $\Omega$  for the PPy and hybrid Ag@PPy nanocomposite electrode, respectively. The charge transfer resistance ( $R_{ct}$ ) can be estimated from the diameter of the semicircle. From the Nyquist plot, the  $R_{ct}$  values of PPy and hybrid Ag@PPy nanocomposite and 0.019 and 0.008  $\Omega$ , respectively. The low ESR and  $R_{ct}$  values of the hybrid Ag@PPy nanocomposite are due to the addition of metallic Ag particles that enhanced the electron hopping system of the PPy, resulting in better utilization of the PPy.

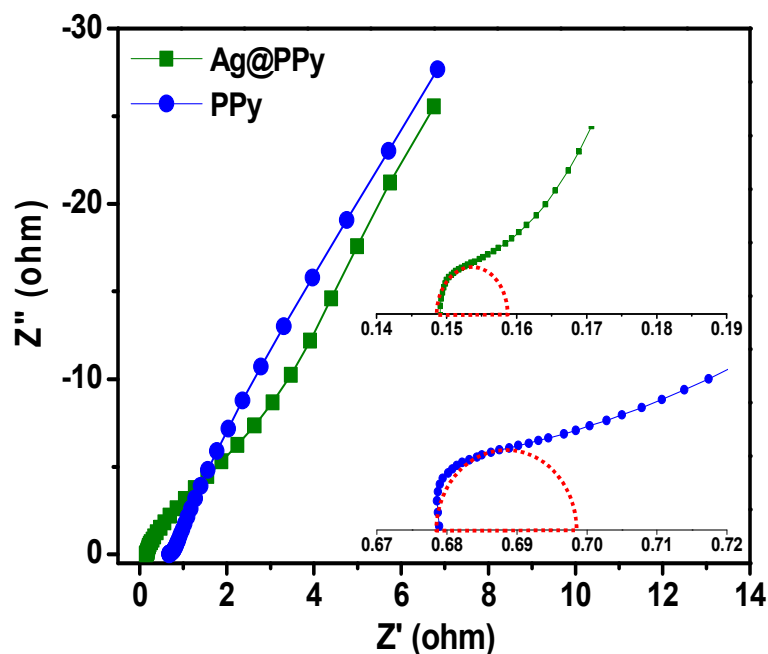


**Fig. 9** Nyquist plots of EIS for PPy and hybrid Ag@PPy nanocomposites. Inset is a magnified portion of the high-frequency region.

### 3.6 Supercapacitor device performance of hybrid Ag@PPy nanocomposite

A three-electrode system has heightened sensitivity to faradaic reaction that can lead to large deviation when projecting the energy storage capability of an electrode material.<sup>39</sup> To the best of our knowledge, there is no report on the electrochemical performance of a two-electrode system fabricated from Ag@PPy nanocomposite. We had made an attempt to fabricate a symmetrical two-electrode cell using hybrid Ag@PPy. Fig. 10a shows the cyclic voltammograms of the symmetric supercapacitor device, which have a rectangular shape within the range of 0 to 0.8 V. The GCD curves of the hybrid Ag@PPy nanocomposite are shown in Fig. 10b. The charging and discharging reveal symmetrical curves, signifying excellent reversibility. The specific capacitance obtained from the discharging curve is calculated to be 161 F g<sup>-1</sup> at a current density of 0.2 A g<sup>-1</sup>. The high specific capacitance is ascribed to the unique hybrid Ag nanoparticles/nanoclusters-decorated PPy nanocomposite. The highly conducting metallic Ag nanoparticles mediate the effective charge migration through the PPy, whilst Ag nanoclusters prevent the restacking of PPy films. Both hybrid Ag nanoparticles/nanoclusters extend the active sites for redox reactions, leading to improved specific capacitance of the hybrid Ag@PPy electrode.

Cycling stability is essential for the commercialization of supercapacitor materials. Fig. 10c shows the capacitance retention as a function of the cycle number at a current density of 0.5 A g<sup>-1</sup> for 1000 cycles. The hybrid Ag@PPy nanocomposite exhibited remarkable cycling stability and retained up to 98.9% of its initial capacitance after 1000 charge/discharge cycles, whereas the PPy electrode only retained 88.8% of capacitance. These results show that the addition of hybrid Ag particles enhanced the cycling stability of PPy. The Ragone plot shows the dependence between the power output and energy density of the symmetric supercapacitor device (Fig. 10d). The energy density of the hybrid Ag@PPy nanocomposite decreased from 13.6 to 2.6 W h kg<sup>-1</sup> as the power density increased from 312 to 5850 W kg<sup>-1</sup>.

On the other hand, the highest energy and power density reached by the PPy electrode is 8.6 W h kg<sup>-1</sup> and 4000 W kg<sup>-1</sup>, respectively. The result demonstrated the improved energy and power density from PPy.

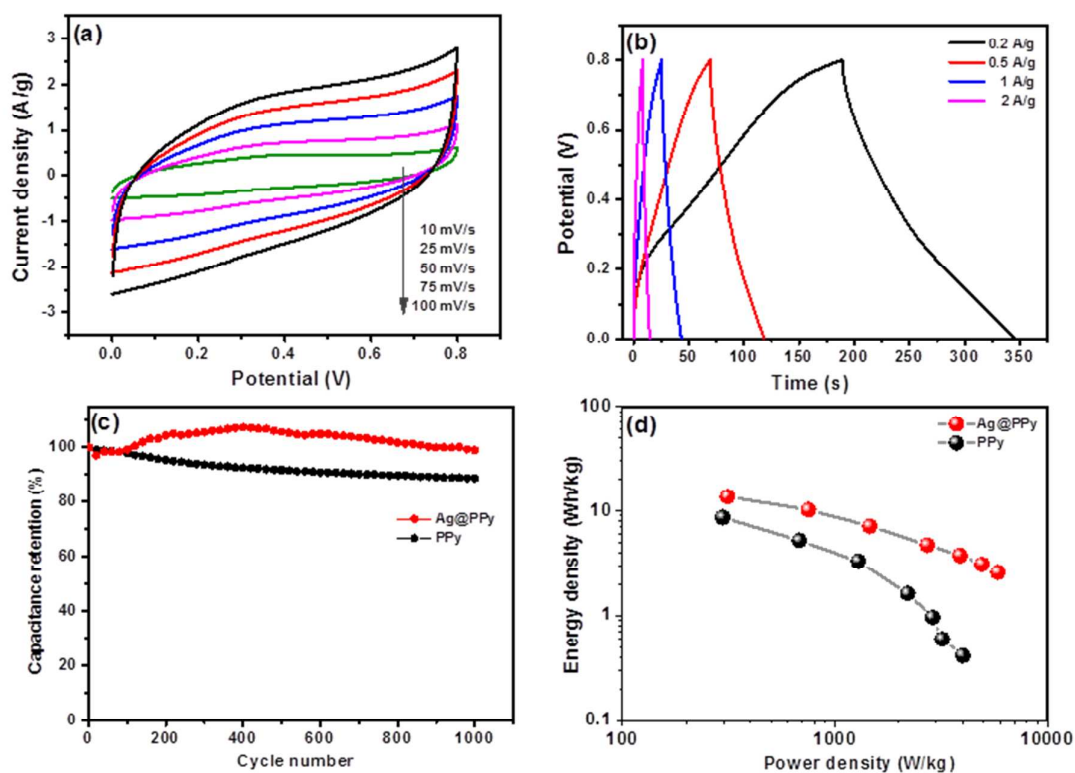


**Fig. 10** (a) CV of the fabricated supercapacitor at various scan rates, (b) GCD curves of fabricated supercapacitor at various current densities, (c) cycling stability, and (d) Ragone plot of the PPy and hybrid Ag@PPy nanocomposite.

#### 4. Conclusion

This work featured a facile strategy for the synthesis of hybrid Ag nanoparticles/nanoclusters-decorated PPy nanocomposites. The FESEM images showed that the best combination of nanoparticles and nanoclusters are formed at the optimized concentration of 0.05 M AgNO<sub>3</sub>. When lower concentration was used, no Ag nanoclusters were found, while at higher concentration, many Ag nanoclusters agglomerated with irregular shapes were observed. The improved capacitance and rate-capability of the hybrid Ag@PPy can be accredited to its unique architecture. Firstly, the 2-4 nm Ag nanoparticles that are evenly distributed on PPy effectively enhanced the electron hopping system of the conjugated PPy, thereby increasing the capacitance of the PPy. Secondly, the larger Ag nanoclusters with a size range of 55-100 nm were uniformly adhered to the PPy film acted as spacers, preventing the PPy films from restacking. Thirdly, the enhanced morphology shortened the transport pathway for electrons and gave better cycling stability. Benefiting from its splendid characteristics, the hybrid Ag nanoparticles/nanoclusters-decorated PPy nanocomposite was shown to exhibit a significantly improved electrochemical performance.

#### Acknowledgements

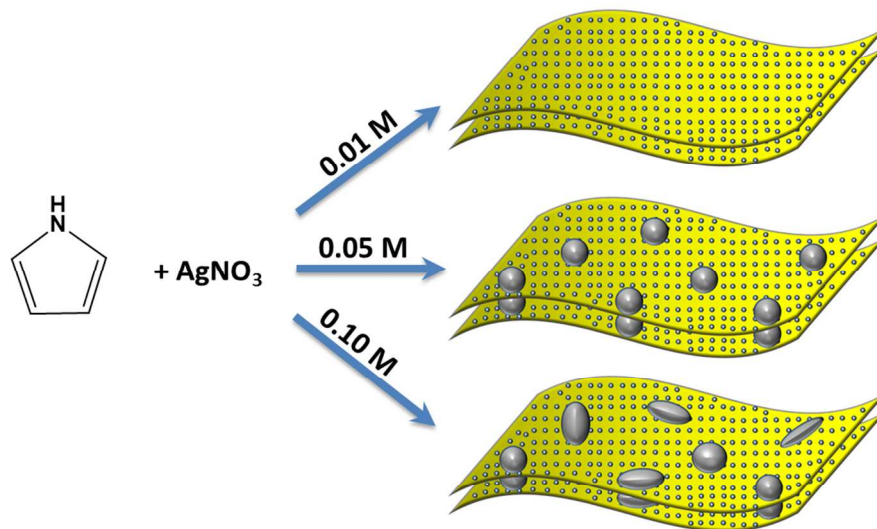
This work was financially supported by a University of Malaya Research Grant Program (RP007/13AFR), the High Impact Research Grant from the Ministry of Higher Education of Malaysia (UM.C/625/1/HIR/MOHE/05) and University Malaya Flagship project (FL017-2011). The authors are grateful to the Synchrotron Light Research Institute, Nakhon Ratchasima, Thailand for the XPS measurements.

## References

1. E. G. Calvo, F. Lufrano, P. Staiti, a. Brigandi, a. Arenillas, and J. a. Menéndez, *J. Power Sources*, 2013, **241**, 776–782.
2. S. Zhang, Y. Li, and N. Pan, *J. Power Sources*, 2012, **206**, 476–482.
3. P. Simon and Y. Gogotsi, *Nat. Mater.*, 2008, **7**, 845–854.
4. J. Shen, C. Yang, X. Li, and G. Wang, *ACS Appl. Mater. Interfaces*, 2013, **5**, 8467–8476.
5. B. Vidhyadharan, N. Khayyriah, M. Zain, I. I. Misnon, R. A. Aziz, J. Ismail, M. M. Yusoff, and R. Jose, *J. Alloys Compd.*, 2014, **610**, 143–150.
6. B. You, L. Wang, N. Li, and C. Zheng, *ChemElectroChem*, 2014, **1**, 772–778.
7. B. E. Conway, V. Birss, and J. Wojtowicz, *J. Power Sources*, 1997, **66**, 1–14.
8. B.-H. Kim, C. H. Kim, K. S. Yang, A. Rahy, and D. J. Yang, *Electrochim. Acta*, 2012, **83**, 335–340.
9. S. Cheng, L. Yang, Y. Liu, W. Lin, L. Huang, D. Chen, C. P. Wong, and M. Liu, *J. Mater. Chem. A*, 2013, **1**, 7709–7716.
10. J.-G. Wang, Y. Yang, Z.-H. Huang, and F. Kang, *Electrochim. Acta*, 2011, **56**, 9240–9247.
11. A. D. Jagadale, V. S. Kumbhar, R. N. Bulakhe, and C. D. Lokhande, *Energy*, 2014, **64**, 234–241.
12. D. S. Patil, S. A. Pawar, R. S. Devan, M. G. Gang, Y. Ma, J. H. Kim, and P. S. Patil, *Electrochim. Acta*, 2013, **105**, 569–577.
13. L. R. Hepowit, K. M. Kim, S. H. Kim, K. S. Ryu, Y. M. Lee, and J. M. Ko, *Polym. Bull.*, 2012, **69**, 873–880.
14. E. Frackowiak, V. Khomenko, K. Jurewicz, K. Lota, and F. Béguin, *J. Power Sources*, 2006, **153**, 413–418.
15. J. Keskinen, S. Tuurala, M. Sjödin, K. Kiri, L. Nyholm, T. Flyktman, M. Strømme, and M. Smolander, *Synth. Met.*, 2015, **203**, 192–199.
16. J. Oh, M. E. Kozlov, B. G. Kim, H.-K. Kim, R. H. Baughman, and Y. H. Hwang, *Synth. Met.*, 2008, **158**, 638–641.
17. J. Wang, Y. Xu, J. Zhu, and P. Ren, *J. Power Sources*, 2012, **208**, 138–143.
18. W. Yao, H. Zhou, and Y. Lu, *J. Power Sources*, 2013, **241**, 359–366.

19. C. Zhou, Y. Zhang, Y. Li, and J. Liu, *Nano Lett.*, 2013, **13**, 2078–2085.
20. W.-H. Guo, T.-J. Liu, P. Jiang, and Z.-J. Zhang, *J. Colloid Interface Sci.*, 2015, **437**, 304–10.
21. M. J. García-Fernández, R. Buitrago-Sierra, M. M. Pastor-blas, O. S. G. P. Soares, M. F. R. Pereira, and A. Sepúlveda-Escribano, *RSC Adv.*, 2015, **5**, 32706–32713.
22. M. Wysocka-Żołopa, E. Grądzka, K. Szymański, and K. Winkler, *Thin Solid Films*, 2013, **548**, 44–51.
23. B. Zhao and Z. Nan, *Mater. Sci. Eng. C*, 2012, **32**, 1971–1975.
24. K. E. Hnida, R. P. Socha, and G. D. Sulka, *J. Phys. Chem. C*, 2013, **117**, 19382–19392.
25. X. Yang, L. Li, and F. Yan, *Sensors Actuators B Chem.*, 2010, **145**, 495–500.
26. C. A. Amarnath, C. E. Hong, N. H. Kim, B.-C. Ku, T. Kuila, and J. H. Lee, *Carbon*, 2011, **49**, 3497–3502.
27. J. Zhu, S. Wei, L. Zhang, Y. Mao, J. Ryu, P. Mavinakuli, A. B. Karki, D. P. Young, and Z. Guo, *J. Phys. Chem. C*, 2010, **114**, 16335–16342.
28. J. Zang and X. Li, *J. Mater. Chem.*, 2011, **21**, 10965–10969.
29. J. Li, L. Cui, and X. Zhang, *Appl. Surf. Sci.*, 2010, **256**, 4339–4343.
30. Z. Gu, C. Li, G. Wang, L. Zhang, X. Li, W. Wang, and S. Jin, *J. Polym. Sci. Part B Polym. Phys.*, 2010, **48**, 1329–1335.
31. J. Cao, Y. Wang, J. Chen, X. Li, F. C. Walsh, J. Ouyang, D. Jia, and Y. Zhou, *J. Mater. Chem. A*, 2015, **3**, 14445–14457.
32. K. F. Babu, P. Dhandapani, S. Maruthamuthu, and M. A. Kulandainathan, *Carbohydr. Polym.*, 2012, **90**, 1557–1563.
33. D. S. Patil, J. S. Shaikh, S. A. Pawar, R. S. Devan, Y. R. Ma, A. V. Moholkar, J. H. Kim, R. S. Kalubarme, C. J. Park, and P. S. Patil, *Phys. Chem. Chem. Phys.*, 2012, **14**, 11886–95.
34. J. Wei, G. Xing, L. Gao, H. Suo, X. He, C. Zhao, S. Li, and S. Xing, *New J. Chem.*, 2013, **37**, 337–341.
35. N. K. Chaki, J. Sharma, A. B. Mandle, I. S. Mulla, R. Pasricha, and K. Vijayamohanam, *Phys. Chem. Chem. Phys.*, 2004, **6**, 1304–1309.
36. O. S. Ivanova and F. P. Zamborini, *J. Am. Chem. Soc.*, 2010, **132**, 70–72.
37. J. Yan, T. Wei, Z. Fan, W. Qian, M. Zhang, X. Shen, and F. Wei, *J. Power Sources*, 2010, **195**, 3041–3045.

38. S. P. Lim, A. Pandikumar, N. M. Huang, and H. N. Lim, *RSC Adv.*, 2014, **4**, 38111–38118.
39. M. D. Stoller and R. S. Ruoff, *Energy Environ. Sci.*, 2010, **3**, 1294–1301.



Schematic representation of the evolution of different Ag@PPy nanocomposites  
205x131mm (150 x 150 DPI)